Inter national Forum on Aeroelasticity and Structural Dynamics
IFASD 2024
17-21 June 2024, The Hague, The Netherlands

TRANSONIC SHOCK OSCILLATIONS IN AN OSCILLATING FINITE SPAN WING

Magan Singh[1] **and Kartik Venkatraman**[1]

[1]Department of Aeorspace Engineering
Indian Institute of Science
Bengaluru, India 560012
magansingh@iisc.ac.in, kartik@iisc.ac.in

Keywords: Transonic buffet, Shock oscillations, Finite span wing, Supercritical airfoil, Benchmark Supercritical Wing (BSCW), Transonic flow.

Abstract: Transonic shock buffet, or shock oscillations due to shock-induced boundary layer separation, over a finite span wing, is of considerable interest from the point of view of fundamental aerodynamics, as well aircraft performance in an overall sense. In this work, we present analyses from numerical URANS simulations of 3D transonic buffet flow over the Benchmark Supercritical Wing, a finite span wing. Transonic buffet is characterized by a broad band of frequencies and aperiodic aerodynamic response. Externally imposed pitch oscillations of the wing, at a frequency close to the transonic buffet frequency of the stationary wing, results in frequency entrainment of the lift and drag coefficients close, but not equal, to the externally imposed frequency. However, the pressure fluctuations as well as streamwise and spanwise pressure wave propagation occur at the transonic buffet frequency. Cross-correlation analysis of the unsteady pressure, on the suction surface, show wave propagation toward the leading edge upstream and downstream of the shock. All streamwise correlation plots confirm the shock oscillations at the buffet frequency of the stationary wing, which is also the frequency of expansion and contraction of the separation bubble.

1 INTRODUCTION

Transonic shock buffet—shock oscillations due to shock-induced boundary layer separation—is well investigated for more than two decades, both through analysis of data from wind tunnel experiments, and high-fidelity numerical simulations. There are excellent review papers on transonic shock buffet by [1, 2, 3], wherein, one can get an overall appreciation of the research on transonic buffet.

Literature on the interaction of transonic buffet and rigid wing oscillation, has to start with the important experimental study by Tijdeman [4, 5]. Tijdeman [4] observed three types of shock motion on the suction surface of the NACA 64A006 wing section due to the effect of sinusoidal trailing edge flap oscillations. Type A is almost sinusoidal shock oscillations with varying strength; shock gains strength during upstream excursion and loses strength during downstream. Type B is similar to Type A, but shock strength variation is significantly greater than Type A, and the shock almost disappears during downstream excursion. Type C is the continuous upstream motion of the shock, gaining in the beginning and losing strength while reaching the leading edge, and eventually merging into the incoming flow. An experimental wind tunnel study of a pitching airfoil by Davis, *et al.* [6], found resonance-like behavior from

the frequency response function of lift coefficient at pitching frequencies close to the buffet frequency of a NACA $64A010$ airfoil at a Mach number of 0.8, $Re = 12 \times 10^6$, and mean AoA of 4°. The behavior is akin to resonance in a single degree of freedom system. Similar resonant behavior was also observed on the OAT15A airfoil with sinusoidal oscillations of trailing edge deflector by [7], where large shock oscillations occurred at excitation frequencies close to the buffet frequency. This behavior of large shock oscillations at excitation close to buffet frequency provides insights into the nature of shock oscillations in dynamic systems. The numerical study by Nitzsche [8] simulated a 2D configuration excited in pitch, streamwise translation, and trailing edge flap oscillations, individually, in transonic flow condition at $M = 0.75$ and $Re = 4.5 \times 10^6$. A URANS simulations using the $k - \omega$ turbulence model was used on a BAC 3-11/RES/$30/21$ airfoil. A resonance-like behavior, as observed in [6], was reported. Raveh [9] reported a lock-in phenomenon between forced heave and self-sustained shock oscillations over a NACA 0012 airfoil. The URANS simulations with the modified $k - \omega$ turbulence model was used for simulating the heave oscillations for varying frequency and amplitude at nominal flow conditions, in this case $M = 0.72$, $Re = 10 \times 10^6$, and AoA 6°. At low amplitude heave oscillations and forcing frequencies away from the buffet frequency, the frequency content of aerodynamic coefficients shows two different peaks of buffet and forced frequency. When the amplitude increases, only the forced frequency peak remains in the frequency content of the aerodynamic response. If the forced frequency is very close to the buffet frequency, the lock-in occurs even at low amplitudes of forced oscillations. The lock-in phenomenon occurs for particular combinations of heave amplitudes and frequency ratios between forced and buffet frequencies, given in [9, Fig. 10].

The focus of the present work is two-fold. First, we present the time domain and frequency domain results for transonic shock buffet over the Benchmarck Supercritical Wing (BSCW). The BSCW is a finite span wing of aspect ratio 2. 3D flow effects are therefore significant. Having established the temporal and frequency characteristics of transonic buffet in this wing, we then proceed to oscillate the wing about its pitching axis at $x/c = 0.3$. The time and frequency domain response of the pitching wing in transonic buffet flow is then analyzed. The boundary layer is assumed to be fully turbulent and therefore URANS simulations using the Spalart-Allmaras (SA) turbulence model closure, with the Edwards-Chandra correction [10], is the numerical tool of choice.

2 METHODS AND TOOLS

Table 1: Flow conditions at $M = 0.8$

Re_c	4×10^6
M	0.8
α	5°
T_∞	300.24 K
Gas	R-134a $\gamma = 1.116$ $R = 81.50$ J/kg-K

The present work focuses on rigid oscillation of the Benchmark Supercritical Wing (BSCW), which is a 3D rectangular planform wing. This wing was used for benchmark studies in the Aeroelasticity Prediction Workshops 1, 2, and 3 (AePW-1,2,3) [11, 12, 13]. The BSCW is shown in Figure 1. It is based on a NASA supercritical airfoil, the NASA SC(2)-0414. The SC(2) designation indicates that the airfoil belongs to a family of second-generation supercrit-

ical airfoils. The 0414 designation indicates that the airfoil is designed with a lift coefficient of 0.4 and a maximum thickness-to-chord ratio of 14% [14]. In AePW-3 [13], the test case $M = 0.8$ was considered to assess the state-of-art in transonic shock buffet and flutter predictions on the BSCW. The wind tunnel test conditions are given in Table 1. A refrigerant gas R-134a is used as a working medium in the tunnel. The boundary layer is assumed to be fully turbulent.

The unsteady Reynolds-averaged Navier-Stokes (URANS) equations are solved numerically. The governing equations are written in vector form as follows.

$$\frac{\partial \boldsymbol{U}}{\partial t} + \boldsymbol{\nabla} \cdot \boldsymbol{F}^c - \boldsymbol{\nabla} \cdot \boldsymbol{F}^v = \boldsymbol{Q}; \quad \text{in} \quad \Omega, \quad t > 0, \tag{1}$$

where $\boldsymbol{U}$ is the vector of state variables $[\rho, \rho\boldsymbol{v}, \rho E]$ and Ω is the fluuid domain. $\boldsymbol{F}^c$ is the vector of convective fluxes and $\boldsymbol{F}^v$ is the vector of diffusive fluxes. These fluxes are defined as

$$\boldsymbol{F}^c = \begin{Bmatrix} \rho(\boldsymbol{v} - \boldsymbol{v}_\Omega) \\ \rho\boldsymbol{v} \otimes (\boldsymbol{v} - \boldsymbol{v}_\Omega) + \bar{\bar{I}}p \\ \rho E(\boldsymbol{v} - \boldsymbol{v}_\Omega) + p\boldsymbol{v} \end{Bmatrix}, \quad \boldsymbol{F}^v = \begin{Bmatrix} . \\ \bar{\bar{\tau}} \\ \bar{\bar{\tau}} \cdot \boldsymbol{v} + \kappa \nabla T \end{Bmatrix}.$$

p is the pressure, ρ is the density, $\boldsymbol{v}$ is the velocity field, $\boldsymbol{v}_\Omega$ is the velocity of moving domain, and E is the total energy per unit mass, $\bar{\bar{\tau}}$ is the viscous stress, $\bar{\bar{I}}$ is the unit matrix, and T is the absolute temperature in Kelvin. $\boldsymbol{Q}$ is the vector of external source terms and expressed as

$$\boldsymbol{Q} = \begin{Bmatrix} q_\rho \\ q_{\rho v} \\ q_{\rho E} \end{Bmatrix}.$$

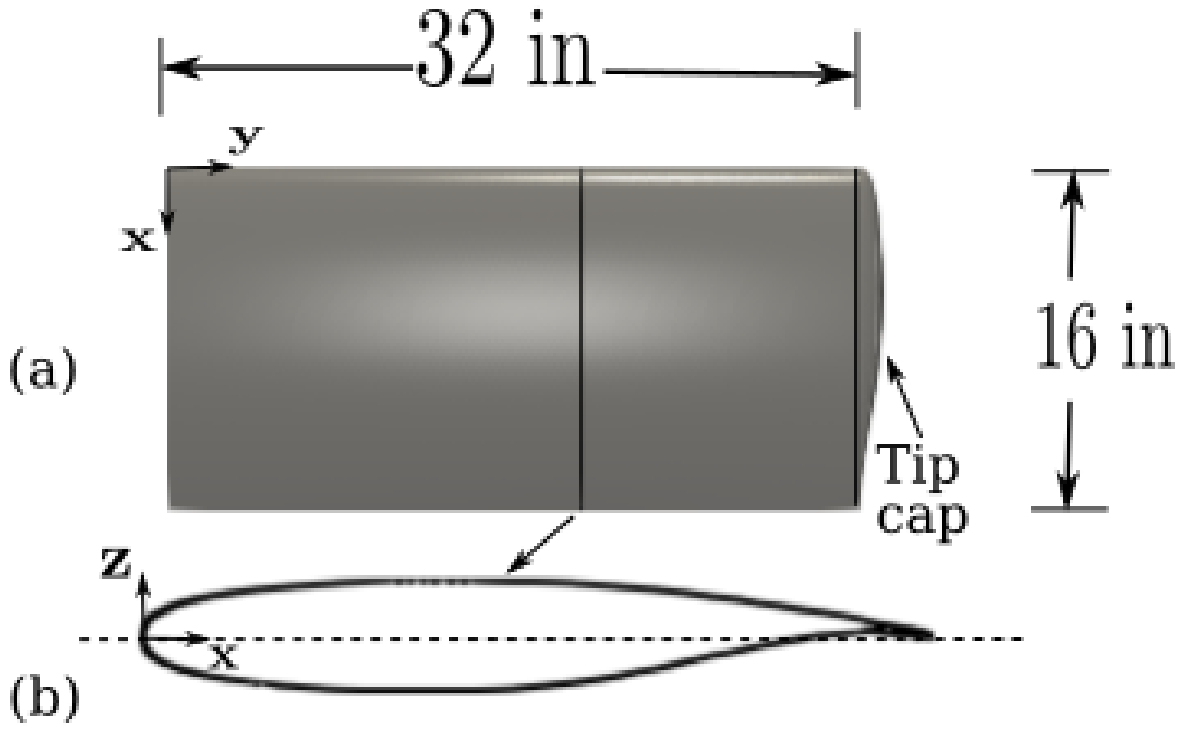

Figure 1: BSCW geometry. (a) Planform area and (b) NASA SC(2)-0414 airfoil.

The viscous stress tensor is

$$\bar{\bar{\tau}} = \mu_{tot}\left(\boldsymbol{\nabla v} + (\boldsymbol{\nabla v})^T - \frac{2}{3}\bar{\bar{I}}(\boldsymbol{\nabla} \cdot \boldsymbol{v})\right), \tag{2}$$

Where an effective viscosity $\mu_{tot} = \mu_l + \mu_t$ based on the Boussinesq hypothesis for turbulent shear stresses in turbulence modeling. Similarly, an effective thermal conductivity relation is given by

$$\kappa = \frac{\mu_l c_p}{Pr_l} + \frac{\mu_t c_p}{Pr_t},$$

Where μ and Pr are the flow viscosity and Prandtl number. Subscripts l and t represent the laminar and turbulent flow. c_p is the specific heat at constant pressure. μ_l is derived from Sutherland's law. μ_t is derived from the turbulence model. A variant of the one-equation Spalart-Allmaras (SA) turbulence model [15], known as the Edwards-Chandra correction [10] is used for closure. This correction improves convergence while maintaining near-wall numerical accuracy, and is shown to predict transonic buffet over an airfoil [16], wing [17], and a full-annulus model of a transonic fan [18].

The fluid is assumed to be a perfect gas and the temperature is expressed using the ideal gas law relation $T = p/\rho R$, where R is the gas constant. The total energy E then is a function of temperature only. Further, for a calorically perfect gas whose internal energy is proportional to temperature, the pressure is given in terms of the internal energy E and fluid velocity v as

$$p = (\gamma - 1)(E - 1/2v^2),$$

where γ is the ratio of specific heats.

The governing Equation 1 is subject to boundary conditions on the wall or surface S, namely the no-slip and adiabatic conditions. The far-field is prescribed as a non-reflecting boundary Γ_∞ in terms of the characteristic $\boldsymbol{W}$.

$$\begin{aligned}
&\boldsymbol{v} = \boldsymbol{v}_\Omega \quad \text{on} \quad S,\\
&\partial_n T = 0 \quad \text{on} \quad S,\\
&\boldsymbol{W}_+ = W_\infty \quad \text{on} \quad \Gamma_\infty,
\end{aligned}$$

where $\boldsymbol{v}_\Omega$ is the velocity of the moving domain.

All simulations were performed using the Stanford University Unstructured (SU2) v7.4.0 suite of codes for fluid, solid, and thermal solvers [19]. In SU2, RANS equations are spatially discretized using a vertex-based finite volume method [20] for an unstructured mesh. RANS and URANS simulations are performed in pseudo time-step for steady flow simulations, and physical time-step for unsteady simulations, respectively. In the RANS equations, the convective flux terms are discretized using the upwind method and evaluated by the flux-difference-splitting scheme of Roe with second-order reconstruction via Monotone Upstream-centered Schemes for Conservation Laws (MUSCL). The van Albada limiter is used to preserve monotonicity in the solution by limiting the gradients. For the turbulence model, convective terms are differenced using a first-order upwind scheme. The state variables $\mathbf{U}$ and their gradients for viscous flux terms of RANS and turbulence models are evaluated at vertices using the weighted least-square method. Then, they are averaged at control volume faces. The equations are temporally discretized using a second-order implicit Euler backward scheme [20]. A dual time-stepping

strategy is used to achieve the time advancement in which the equations are converged iteratively to a reasonable lower order of magnitude in pseudo-time at every physical time step. Further, the set of linear equations is solved for state variables using the Generalized Minimal Residual (GMRES) linear solver.

BSCW unstructured grids of different sizes based on mesh refinement are available from [12]; those are used for URANS simulations in SU2. The grid comprises of three types of elements: tetrahedrons, prisms, and pyramids. Prism elements are very close to the wing's surface, tetrahedrons are far away from the surface, and pyramids are near the surface between prism and tetrahedron elements. The grid topology and far-field boundary at around $100c$, where c is the chord length, from the wing's surface is shown in Figure 2a. The boundary conditions are set on grid boundaries. The symmetry, far-field, and no-slip adiabatic wall conditions are set on the symmetry plane, cuboid far-field boundary, and BSCW surface as shown in Figure 2b. There were three grid resolutions available for simulation: coarse with $y+ = 1$, medium with $y+ = 2/3$, and fine with $y+ = 4/9$. Subsequent to grid convergence and time convergence study, a medium grid was found adequate with a time-step of $\Delta t = 1 \times 10^{-6}$ seconds.

The forced pitching oscillation about the pitching axis at 30% chord is a sinusoidal motion about the 5° mean AoA with amplitude 1° at 20 Hz as shown in Figure 3. This is simulated in SU2 [21] using the unsteady RANS model. URANS simulations are restarted from the last iteration of the steady RANS simulation on stationary BSCW configuration at the same $M = 0.8$ flow conditions. The choice of 20 Hz forced excitation frequency is based on it being very close to the 3D buffet frequency of 19.53 Hz, or St 0.0590, at $M = 0.8$ flow conditions on the stationary BSCW.

3 RESULTS AND DISCUSSION

THe C_L and C_D oscillations in Figure 4a and Figure 4b, respectively, are almost sinusoidal and in phase with forcing function $\alpha(t)$ of the pitching motion. Therefore, the power spectral density (PSD) of C_L in Figure 4c shows a peak at 19.07 Hz or St 0.0576, which is close to the forcing frequency of 20 Hz. The PSD of C_L was computed using the Welch method [22] from a set of 168500 samples with a sampling frequency 10^6 samples/s in a time interval of 0.165 seconds of steady-state solution data record, as marked in Figure 4a. The sample length was divided into 2 overlapping segments with 50% overlap, and each segment is windowed using a

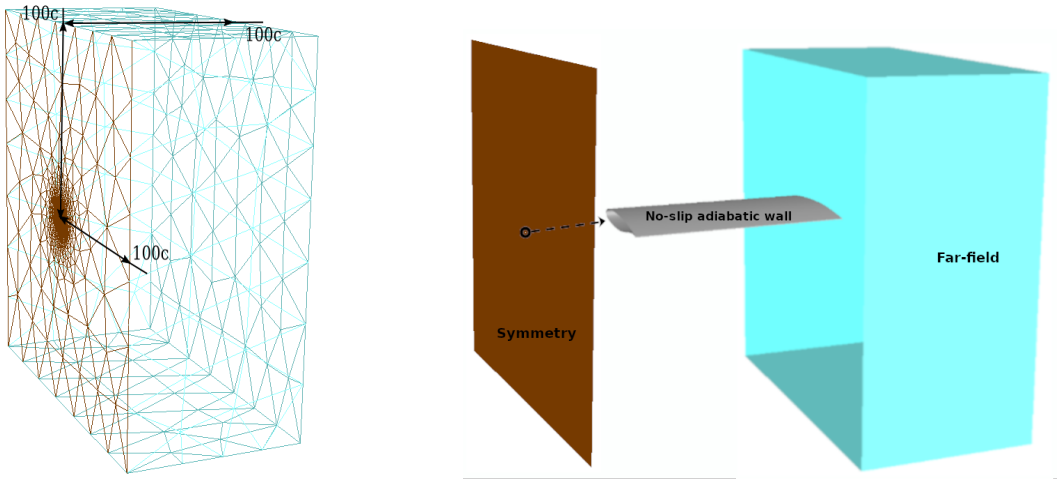

(a) Grid topology (b) Boundary conditions

Figure 2: BSCW unstructured grid and boundary conditions

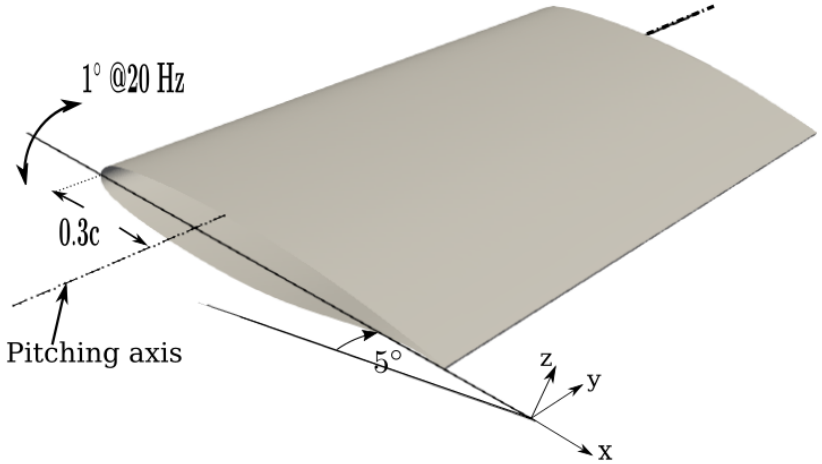

Figure 3: Schematic diagram of BSCW pitching about 30% of chord.

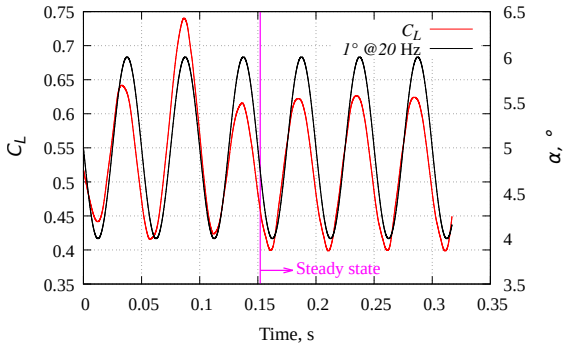

(a) C_L in pitch oscillation

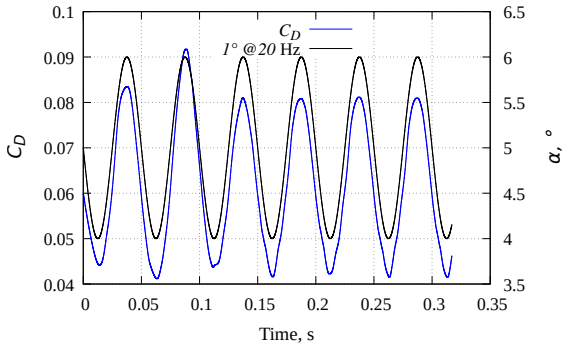

(b) C_D in pitch oscillation

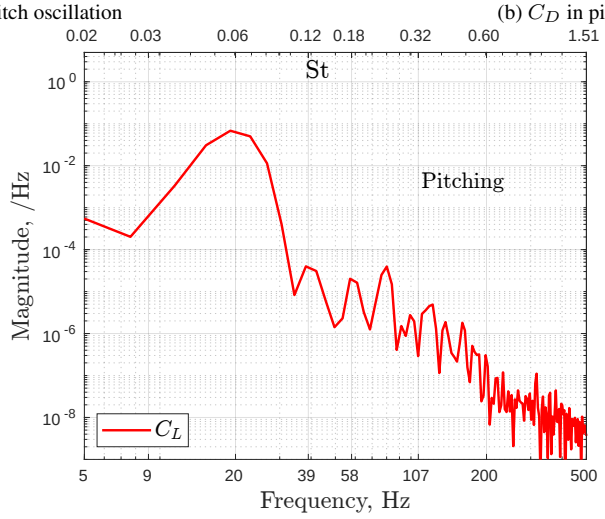

(c) PSD of C_L in pitch oscillation

Figure 4: Coefficient of lift C_L and drag C_D, and PSD of C_L, of pitching BSCW.

Hamming window. Notice that the PSD of the C_L, in Figure 4c, also shows the harmonics of the fundamental frequency of 19.07 Hz; the first at 38.14 Hz, the second at 57.21 Hz, and the third at 76.28 Hz. The fundamental frequency of 19.07 Hz, determined from the PSD, in the forced aerodynamic response, due to a 20 Hz pitch excitation is similar to what was observed in the lock-in phenomenon described by [9] for 2D configurations. Frequency entrainment is characteristic of a certain class of nonlinear dynamical systems that have limit cycles as equilibrium solutions.

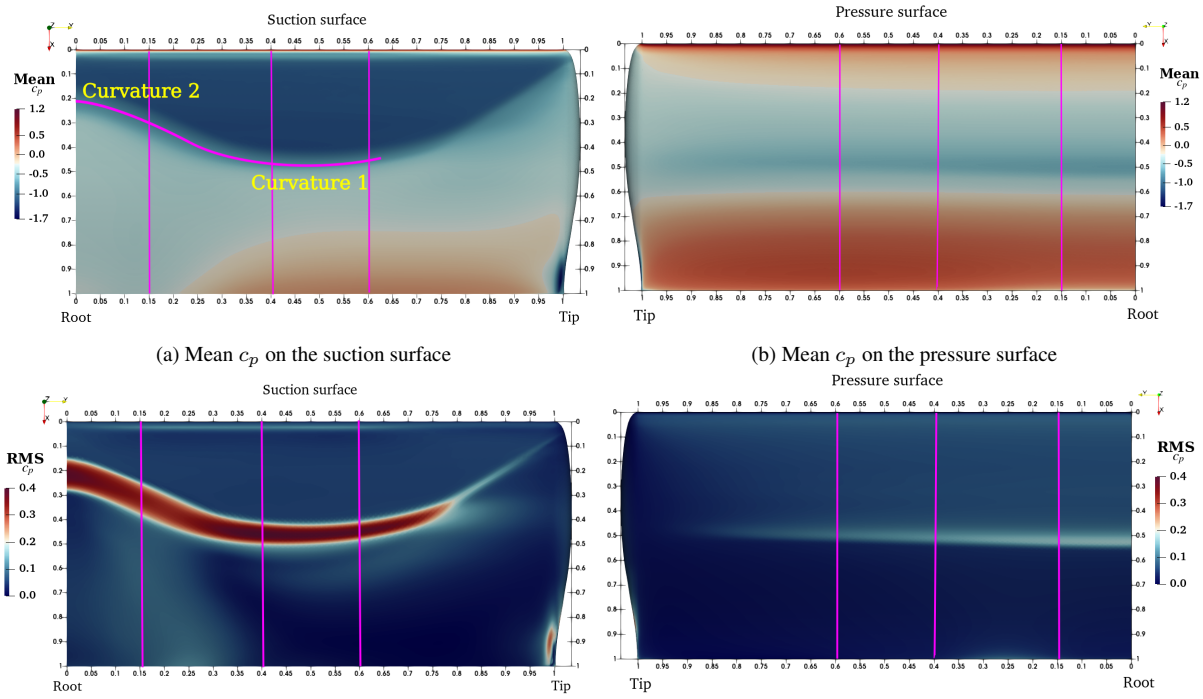

(a) Mean c_p on the suction surface

(b) Mean c_p on the pressure surface

(c) RMS c_p on the suction surface

(d) RMS c_p on the pressure surface

Figure 5: Mean c_p RMS c_p surface distributions over the pitching wing.

Mean and RMS c_p contours on the suction and pressure surfaces are included in Figure 5. Since the wing is pitching about 30% of the chord, as shown in Figure 3, grid nodes on the surface change their position as well as coordinates. Therefore, the mean and standard deviation or RMS of c_p are computed by considering pressure fluctuations on every node in a Lagrangian frame for the time interval of steady-state response marked in Figure 4a. These statistical results on the wing surface, as well as on spanwise sections, are shown as function of grid coordinates at the mean AoA of $5°$. For the pitching wing, the two curvatures along the span, on the mean and RMS c_p in Figure 5a and Figure 5c, respectively, typically decrease in comparison to the stationary wing. The curvature of the separation line is less pronounced relative to that of the stationary wing. Thus, the locus of chordwise shock locations along the span resembles approximately a curve with a single dominant curvature. In the case of the stationary wing, the separation line consists of two dominant curvatures. The influence of pitching dynamics mainly affect the wing's root region inboard of the 20% span. On the pressure surface, mean c_p contours in Figure 5b for pitching wing do not show significant change relative to that of the stationary wing. But, RMS c_p contours on the pressure surface, in Figure 5d, for the pitching wing, shows higher pressure fluctuations in the shock region along the span than relative to that of the stationary wing. The higher pressure fluctuations are most likely caused by the forced pitching excitation, which impart energy to the shock excursion, and therefore increase the pressure fluctuations and buffet amplitude in the excursion region.

Transonic shock buffet over airfoils and wings is associated with pressure wave propagation in the unsteady flow-field. Studies [23, 24] have used cross-correlation analysis to observe pressure wave propagation, and proposed a feedback loop mechanism to explain transonic shock buffet over an airfoil. Similarly, in order to study streamwise and spanwise pressure wave propagation in 3D shock buffet over a finite span swept wing have used cross-correlation analysis [25, 26]. The cross-correlation of the fluctuating component c_p', of the coefficient of pressure c_p is computed on the wing suction and pressure surfaces. These cross-correlations are computed

streamwise at two spanwise stations, and also spanwise along a line at a constant chordwise location, typically at the most downstream location of the shock. For discrete points in space and time, the two-point cross-correlation is expressed for signals of a finite length t as

$$\hat{R}_{s_1 s_2}(\tau) = \sum_t [s_1(t) s_2(t+\tau)] \delta t, \tag{3}$$

where δt is the time interval between two consecutive steps of the signal, $s_1(.)$ and $s_2(.)$ are the time varying signals at two spatial locations, and τ is the correlation interval or time-lag. Here, the correlation is computed along streamwise, or chordwise, locations, as well as spanwise stations, on the suction and pressure surface as

$$R_{c'_{p_r} c'_{p_i}}(X, \tau) = \frac{\hat{R}_{c'_{p_r} c'_{p_i}}(\tau)}{\sqrt{\hat{R}_{c'_{p_r} c'_{p_r}}(0)\ \hat{R}_{c'_{p_i} c'_{p_i}}(0)}}, \tag{4}$$

where c'_{p_r} and c'_{p_i} are the fluctuating component of c_p at a reference station r and at a varying location i, either along the chord or along the span. Here, $R_{c'_{p_r} c'_{p_i}}$ is a function of position vector X and time lag τ. For brevity, we will represent $R_{c'_{p_r} c'_{p_i}}$ as R_{ri}. The horizontal distance between the slopes of two consecutive maxima, or minima, on the τ axis, will denote the time period, or its inverse the frequency, of these waves. Given the phase speed and the time period, one can then calculate the wavelength of the pressure disturbance. Streamwise and spanwise correlation contours are in direct relation with temporal c_p distribution. Later these will be correlated with skin friction line distribution on the surface of the wing.

Streamwise correlations and temporal c_p distributions on both surfaces are shown for 15% span only, although streamwise correlations were computed at 40% and 60% span also. On the

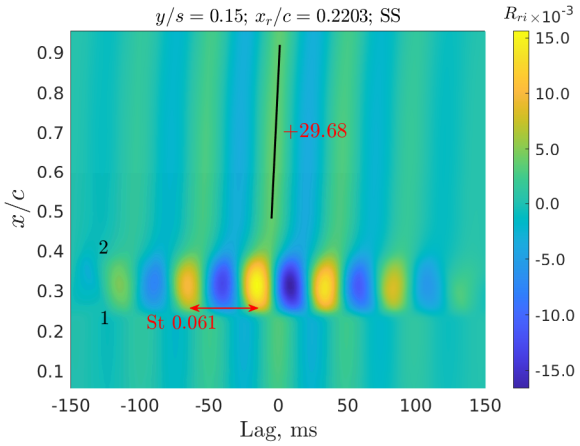

(a) R_{ri} on the suction surface

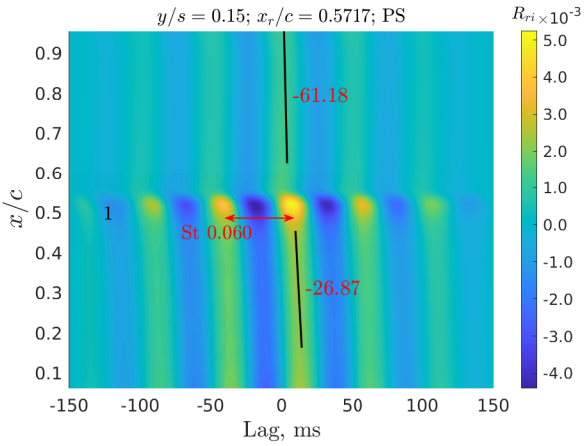

(b) R_{ri} on the pressure surface

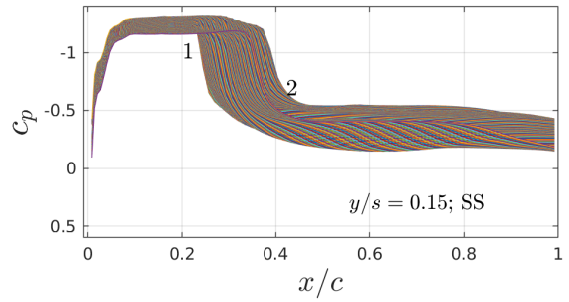

(c) Temporal c_p distribution on the suction surface

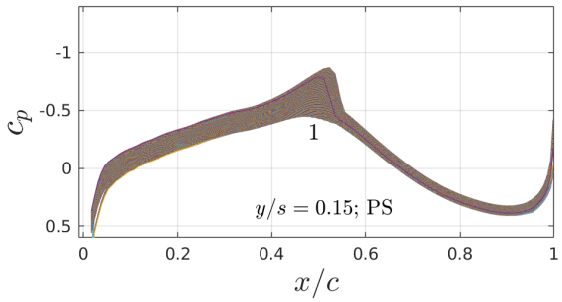

(d) Temporal c_p distribution on the pressure surface

Figure 6: Streamwise correlations R_{ri} and temporal c_p distribution at 15% span.

suction side, the reference locations in computing streamwise correlations are immediately upstream of the shock excursion region, such as x_r/c 0.2203, 0.3622, and 0.3556 for 15%, 40%, and 60% spans, respectively. On the pressure side, the reference locations are immediately downstream of the shock excursion region, such as $x_r/c = 0.5717$, 0.5622, and 0.5503 for 15%, 40%, and 60% spans, respectively. Correlation magnitudes at all three span locations are of the same $\mathcal{O}$(-3) order on both sides, although the correlation magnitude on the suction side is higher than that on the pressure side. Streamwise correlations consist of a regular occurrence of local maxima and minima correlation R_{ri} values in the shock excursion regions on both surfaces. The frequency of shock excursions on both surfaces is the frequency of wave propagation in other chordwise regions. In all correlation plots, the shock excursion, buffet, or wave propagation frequencies are almost the same as 19.53 Hz or St 0.0590 obtained from PSDs of c_p fluctuation at chord points at 15% span.

Streamwise correlations and temporal c_p distributions on both surfaces at 15% span are given together in Figure 6. Figure 6a is marked at two stations along the chord, and relates to the temporal c_p distribution in Figure 6c. Station 1 at $\approx 0.23c$ and station 2 at $\approx 0.42c$ are immediately upstream and downstream of the shock excursions, respectively. Downstream of the shock excursion, disturbance propagates at speed a 29.68 m/s toward the trailing edge, which is not seen at other span stations. This is since the 15% span station is in the flow-separated region, while others are in the flow-attached region downstream of a bubble along the span. The flow-separated region near the root consists of foci and saddle critical points traveling periodically in both streamwise and spanwise directions.

On the pressure side, streamwise correlation in Figure 6b and temporal c_p distribution in Fig-

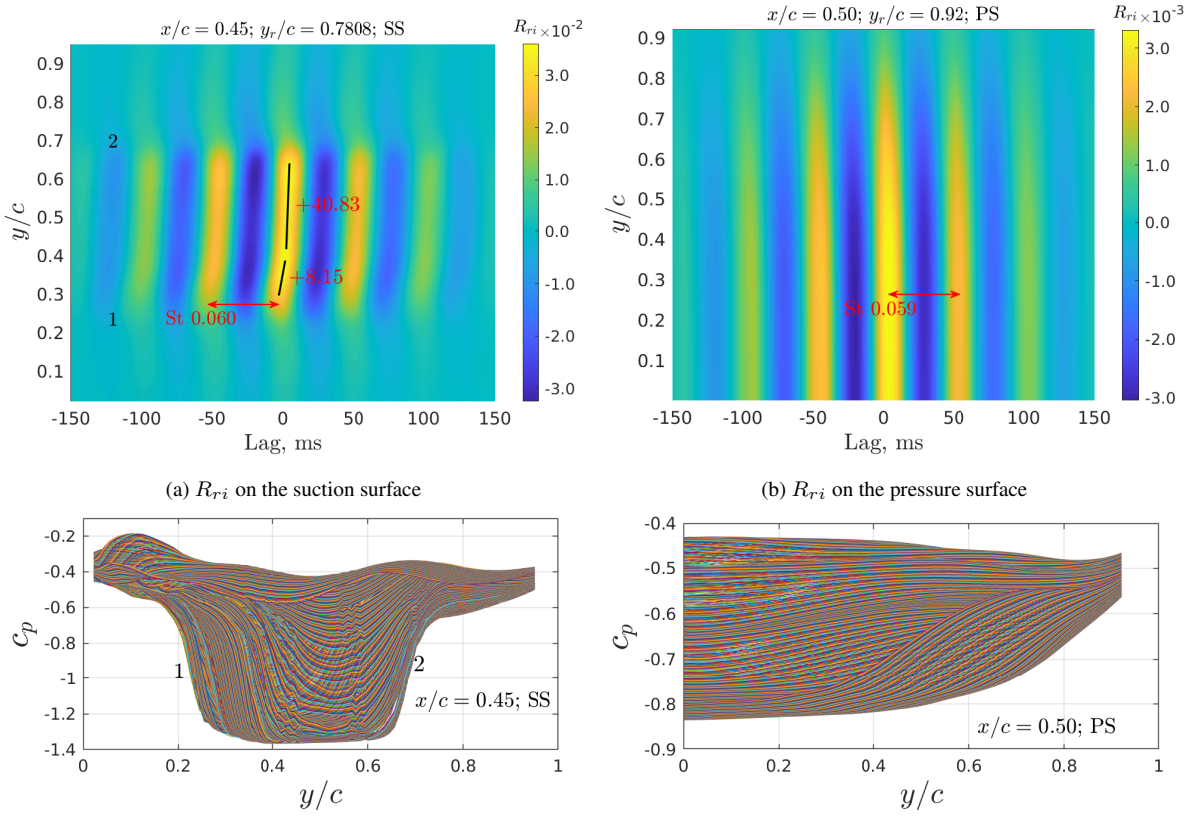

(a) R_{ri} on the suction surface

(b) R_{ri} on the pressure surface

(c) Temporal c_p distribution on suction surface

(d) Temporal c_p distribution on pressure surface

Figure 7: Spanwise correlations R_{ri} and temporal c_p distribution in the shock excursion region.

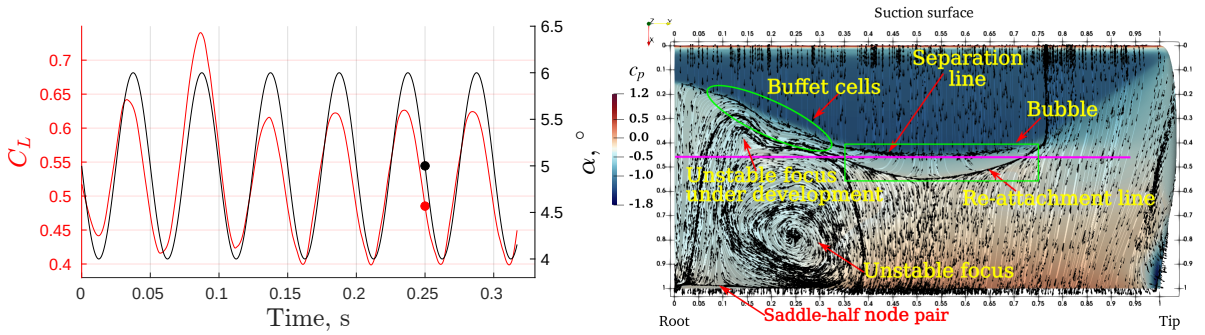

(a) C_L at time instant $t = 0.25$ sec

(b) Instantaneous skin friction lines at $t = 0.25$ sec

Figure 8: Propagation of buffet cells at time instant $t = 0.25$ sec.

ure 6d the station of interest is marked 1 at the mean shock location $\approx 0.50c$. Inboard wave propagation, upstream and downstream of 1 are -61.18 and -26.87 m/s, respectively; an average speed -44.03 m/s of both can be assumed because of minor shock strength on the pressure side, traveling inboard from the trailing to the leading edge. Flow is attached to the pressure surface everywhere, so there is no chance of critical points. Wave propagation on the pressure side is due to two factors. First is the refraction of wave propagation at the trailing edge, traveling from the suction side, which was also observed by [27]. Second is the higher pressure fluctuations due to the forced pitching motion, which results in a higher magnitude of correlation.

Spanwise correlations accompanying temporal c_p distributions along spanwise lines at 45% chord on the suction side and 50% chord on the pressure side are shown in Figure 7. These chord locations at 45% and 50% suction and pressure surface, respectively, of the wing are of lines passing through the shock excursion region. These chord locations were chosen to consider the effect of shock excursion on wave propagation. Spanwise correlation and temporal c_p distribution on the suction side, in Figure 7, at 45% chord, are marked for locations where there is a change pressure perturbation, whereas on the pressure surface, there is no such marking. Correlation and temporal c_p distribution plots on the suction side, in Figure 7a and Figure 7c, respectively, are marked at spanwise stations 1 and 2. Both these stations enclose the high pressure fluctuation region in Figure 7c, which is reflected in the high magnitude of correlation values in the same spanwise region. Stations 1 and 2 are at $\approx 0.21s$ and $\approx 0.71s$ spanwise locations. For correlation in Figure 7a on the suction side, outboard wave propagation speeds are 8.15 and 40.83 m/s between marks 1 and 2. Within this spanwise region, propagation speeds 40.83 m/s is for 25% of the span from 40 to 65% spans, and 8.15 m/s is for 15% of the span from 25 to 40% spans. This outboard propagation spanwise region between 1 and 2, at 45% chord, is the region of the separation bubble.

Outward propagation in the spanwise region initiates near the vicinity of the wing root, where unstable foci generate disturbance and drive it in both, spanwise and streamwise directions. Wave propagation or buffet cells travel along an inclined separation line near the root, not along the straight horizontal span-wise line drawn at 45% chord shown in Figure 8. Figure 8 shows C_L at time instant 0.25 sec together with the instantaneous skin friction line contours on the suction surface. Note the buffet cells near the wing root, as well as the separation bubble formed in the mid-span region of the wing. Propagation of buffet cells on the separation line occurs periodically in each cycle. Further, the correlation on the suction side shows a propagation frequency of 19.85 Hz or St 0.060, which can also be interpreted as a frequency of bubble growing and contracting in the spanwise region between points 1 and 2 as shown in Figure 7c.

On the pressure side, pressure correlations are shown in Figure 7b and temporal c_p distribution in Figure 7d. Wave propagation is negligible as the locus of local maxima is almost at right angles. The same can be understood from temporal c_p distribution on the pressure side. The wave propagation frequency of 19.53 Hz, or St 0.059, from the correlation plot, is of shock excursion along the spanwise line at 50% chord. The correlation for the pitching wing shows a periodicity of shock excursions; however this periodicity is absent in the correlation for the stationary wing.

4 CONCLUSIONS

The forced pitching oscillation of BSCW at a frequency of 20 Hz with 1° amplitude about a 5° mean AoA is simulated using the unsteady Reynolds-averaged Navier-Stokes fluid model with Edwards-Chandra corrected SA turbulence closure. The buffet frequency for the stationary wing for the same configuration and flow conditions, measured in terms of the lift and drag coefficient, is nominally 19.53 Hz or $St = 0.0590$. The aerodynamic response is broad-band in the frequency range of $19 - 25$ Hz with a minor peak at 19.53 Hz. This is denoted as the buffet frequency. The time domain aerodynamic response is also aperiodic. The aerodynamic response of the pitching wing, in terms of C_L and C_D, in the frequency domain, shows a well defined peak at 19.07 Hz, and secondary peaks at harmonics of this fundamental frequency. The time domain response is harmonic with the fundamental frequency dominating. Note that the fundamental aerodynamic response frequency is close to the frequency of excitation, but not exactly the same. This is typical of frequency entrainment in nonlinear dynamical systems that possess periodic equilibrium solutions known as limit cycles. Cross-correlation analysis was carried out to compute the wave propagation speed and direction along streamwise and spanwise lines on the suction and pressure surfaces of forced pitching BSCW. On the suction surface, only streamwise correlation at 15% span shows wave propagation toward the trailing edge, in the separated region downstream of the shock. On the pressure surface, correlations at 15% and 40% spans show wave propagation toward the leading edge upstream and downstream of the shock, and correlation at 60% span shows wave propagation toward the leading edge only upstream of the shock. All streamwise correlation plots confirm the shock oscillations at almost the buffet frequency of 19.53 Hz, which is also the frequency of expansion and contraction of the separaation bubble. Therefore, the pressure fluctuations oscillate at a frequency equal to that of shock oscillations, namely 19.53 Hz, in a stationary wing, while the lift and drag oscillations occur at a frequency of 19.07 Hz, that is the entrainment frequency of the forced nonlinear dynamical system.

REFERENCES

[1] Lee, B. (2001). Self-sustained shock oscillations on airfoils at transonic speeds. *Progress in Aerospace Sciences*, 37(2), 147–196. doi:https://doi.org/10.1016/S0376-0421(01)00003-3.

[2] Giannelis, N. F., Vio, G. A., and Levinski, O. (2017). A review of recent developments in the understanding of transonic shock buffet. *Progress in Aerospace Sciences*, 92, 39–84. doi:https://doi.org/10.1016/j.paerosci.2017.05.004.

[3] Gao, C. and Zhang, W. (2020). Transonic aeroelasticity: A new perspective from the fluid mode. *Progress in Aerospace Sciences*, 113, 100596. doi:https://doi.org/10.1016/j.paerosci.2019.100596.

[4] Tijdedman, H. (1977). *Investigations of the transonic flow around oscillating airfoils*. Ph.D. thesis, National Aerospace Laboratories (NLR), Amsterdam, Netherlands.

[5] Tijdedman, H. and Seebass, R. (1980). Transonic flow past oscillating airfoils. *Annual Reviews of Fluid Mechanics*, 12, 181–222.

[6] Davis, S. S. and Malcolm, G. N. (1980). Transonic shock-wave/boundary-layer interactions on an oscillating airfoil. *AIAA Journal*, 18(11), 1306–1312.

[7] Despré, C., Caruana, D., Mignosi, A., et al. (2000). Buffet active control - Experimental and numerical results. In *Symposium RTO-Active control technology for enhanced performance operational capabilities of aircraft*.

[8] Nitzsche, J. (2009). A numerical study on aerodynamic resonance in transonic separated flow. In *International Forum on Aeroelasticity and Structural Dynamics 2009 (IFASD 2009)*. Seattle, USA.

[9] Raveh, D. E. (2009). Numerical study of an oscillating airfoil in transonic buffeting flows. *AIAA Journal*, 47(3), 505–515.

[10] Edwards, J. R. and Chandra, S. (1996). Comparison of eddy viscosity-transport turbulence models for three-dimensional, shock-separated flowfields. *AIAA journal*, 34(4), 756–763.

[11] NASA (2015). Aeroelasticity prediction workshop-1. `https://c3.ndc.nasa.gov/dashlink/static/media/other/AEPW_legacy.htm`.

[12] NASA (2016). Aeroelastic prediction workshop-2. `https://nescacademy.nasa.gov/workshops/AePW2/public/`.

[13] NASA (2019). Aeroelastic prediction workshop-3. `https://nescacademy.nasa.gov/workshops/AePW3/public`.

[14] Dansberry, B. (1992). Dynamic characteristics of a benchmark models program supercritical wing. In *33rd Structures, Structural Dynamics and Materials Conference*. p. 2368.

[15] Spalart, P. and Allmaras, S. (1994). A one-equation turbulence model for aerodynamic flows. In *Recherche Aerospatiale, No. 1*. pp. 5–21.

[16] Poplingher, L., Raveh, D. E., and Dowell, E. H. (2019). Modal analysis of transonic shock buffet on 2d airfoil. *AIAA Journal*, 57(1), 2851–2866.

[17] Iovnovich, M. and Raveh, D. E. (2015). Numerical study of shock buffet on three-dimensional wings. *AIAA Journal*, 53(2), 449–463. doi:10.2514/1.J053201.

[18] Majhi, J. R. and Venkatraman, K. (2023). Numerical simulation of transonic buffet in an axial-flow fan. In *AIAA Aviation Forum 2023, June 12-16, 2023; San Diego, USA*. doi:https://doi.org/10.2514/6.2023-4082. Paper;Presentation.

[19] Economon, T. D., Palacios, F., Copeland, S. R., et al. (2016). Su2: An open-source suite for multiphysics simulation and design. *AIAA Journal*, 54(3), 828–846. doi:10.2514/1.J053813.

[20] Palacios, F., Alonso, J., Duraisamy, K., et al. (2013). Stanford university unstructured (su 2): an open-source integrated computational environment for multi-physics simulation and design. In *51st AIAA aerospace sciences meeting including the new horizons forum and aerospace exposition*. p. 287.

[21] SU2 (2023). Stanford University Unstructured (SU2).

[22] Welch, P. (1967). The use of fast fourier transform for the estimation of power spectra: a method based on time averaging over short, modified periodograms. *IEEE Transactions on audio and electroacoustics*, 15(2), 70–73.

[23] Lee, B. (1990). Oscillatory shock motion caused by transonic shock boundary-layer interaction. *AIAA journal*, 28(5), 942–944.

[24] Deck, S. (2005). Numerical simulation of transonic buffet over a supercritical airfoil. *AIAA journal*, 43(7), 1556–1566. doi:10.2514/1.9885.

[25] Dandois, J. (2016). Experimental study of transonic buffet phenomenon on a 3d swept wing. *Physics of Fluids*, 28, 016101.

[26] Paladini, E., Dandois, J., Sipp, D., et al. (2018). Analysis and comparison of transonic buffet phenomenon over several three-dimensional wings. *AIAA Journal*, 57(1), 379–396.

[27] Jacquin, L., Molton, P., Deck, S., et al. (2009). Experimental study of shock oscillation over a transonic supercritical profile. *AIAA journal*, 47(9), 1985–1994. doi:10.2514/1.30190.

COPYRIGHT STATEMENT